

Multi-mode excitation drives disorder during the ultrafast melting of a C_4 -symmetry-broken phase

Daniel Perez-Salinas^{1*}, Allan S. Johnson^{1*}, D. Prabhakaran², Simon Wall^{1,3}

¹*ICFO – The Institute of Photonics Sciences, The Barcelona Institute of Science and Technology, 08860, Castelldefels, Barcelona, Spain*

²*Department of Physics, Clarendon Laboratory, University of Oxford, Oxford OX1 3PU, United Kingdom*

³*Department of Physics and Astronomy, Aarhus University, Ny Munkegade 120, 8000 Aarhus C, Denmark*

**Equal contribution*

Abstract

Spontaneous C_4 -symmetry breaking phases are ubiquitous in layered quantum materials, and often compete with other phases such as superconductivity. Preferential suppression of the symmetry broken phases by light has been used to explain non-equilibrium light induced superconductivity, metallicity, and the creation of metastable states. Key to understanding how these phases emerge is understanding how C_4 symmetry is restored. A leading approach is based on time-dependent Ginzburg-Landau theory, which explains the coherence response seen in many systems. However, we show that, for the case of the single layered manganite $\text{La}_{0.5}\text{Sr}_{1.5}\text{MnO}_4$, the theory fails. Instead, we find an ultrafast inhomogeneous disordering transition in which the mean-field order parameter no longer reflects the atomic-scale state of the system. Our results suggest that disorder may be common to light-induced phase transitions, and methods beyond the mean-field are necessary for understanding and manipulating photoinduced phases.

Introduction

As new light-induced hidden phases are discovered with properties like anomalous metallicity¹⁻³ and superconductivity^{4,5}, understanding how light can manipulate quantum materials is increasingly important⁶. Materials which show an instability between a C_4 symmetry-broken phase and a metallic or superconducting state in equilibrium appear especially likely to host such phases⁷, and it is argued that photoexcitation suppresses the symmetry-broken phase⁸, enabling the “hidden phase” to emerge before thermalization. For example, light-induced superconducting states have been attributed to preferential melting of stripe^{4,5} or charge density wave⁹ order, while insulator-metal phase transitions have been explained by selective melting of charge and orbital order¹⁻³. However, the process by which the symmetry is restored following photoexcitation, and how energy couples to the different degrees of freedom, remains controversial, and is critical for understand the microscopic origin of emergent transient and metastable phases in these materials.

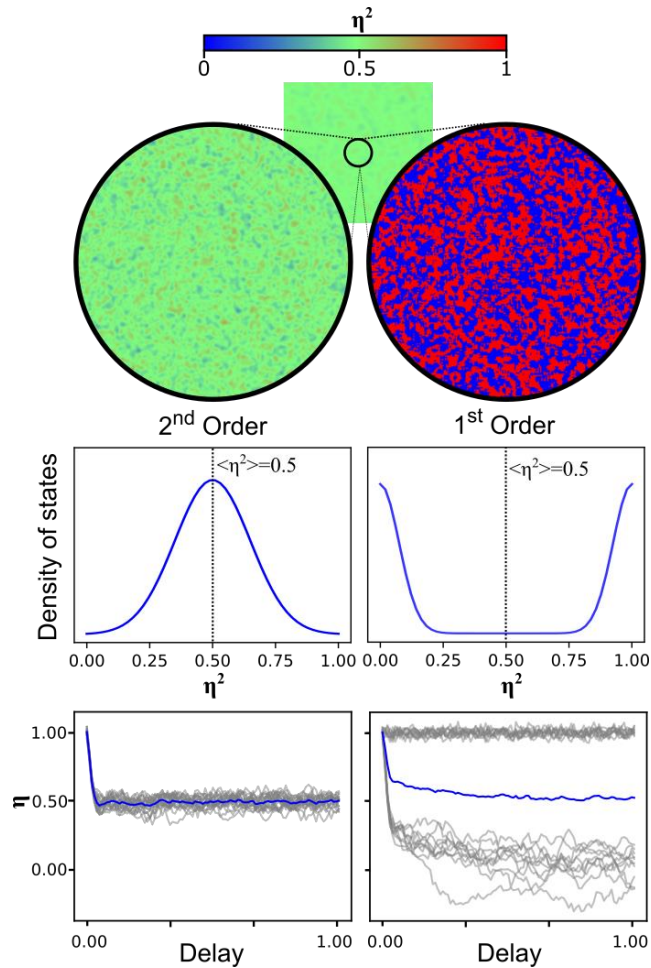


Figure 1. Beyond Ginzburg-Landau for atomic scale dynamics. A schematic of a spatially resolved order parameter measured on the mesoscale after photo-excitation during an ultrafast disordering transition for a 2nd order transition (left) and 1st order (right). An average value of $\eta^2=0.5$ is measured for the order parameter in both cases. For second-order transitions the order parameter can take a continuum of values, and transitioning from the meso-scale to the atomic scale preserves the order parameter. The system is uniformly partially melted with a local order parameter distribution peaked at 0.5. The local dynamics are similar to the average, despite the disorder. However, for first-order transitions, the order parameter can take one of two values (0, 1). In this case, the atomic scale view shows a bimodal distribution peaked at either zero or 1, and no part of the system is at the averaged value, nor are the dynamics of the average order parameter reflected in the averaged response. Such distributions require physics beyond the mean-field to describe.

The difficulty arises because solids have many degrees of freedom making it hard to track them all on the ultrafast timescale, particularly the order parameter. Currently, the prevailing picture is a mean-field description, time-dependent Ginzburg-Landau (TDGL) theory, where the system is coarse-grained and partitioned into the order parameter and a potential determined by the other degrees of freedom. It is assumed that light transiently perturbs this potential, generating a force on the order parameter, and its subsequent evolution captures the key observed dynamics. TDGL makes several clear predictions when damping is minimal. Photoexcitation shifts the minima for the order parameter towards zero. If this shift is prompt, and small, the order parameter coherently oscillates about a new and reduced value¹⁰.

The potential minimum evolves continuously with excitation until it reaches zero, while simultaneously softening, leading to critical slowing down of the order parameter dynamics¹¹. At higher fluences, the potential minimum is fixed at the high symmetry point, but the potential can still change and the order parameter can evolve coherently such that the system can overshoot and cross-over from one ordered domain to another, with an order parameter of opposite sign^{10,12,13} and oscillates about the high symmetry state. Such underdamped and coherent systems are amenable to coherent control¹⁴, and this formulation has been applied to a range of systems, including the manganites¹⁵, suggesting a universal behavior in quantum materials and a way to realize non-thermal states.

While the vast majority of ultrafast phase transitions measured to date have been interpreted in this coherent framework^{10–16}, incoherent transitions have also been reported. The ultrafast phase transition in VO₂ was shown to result from broad distribution of modes, rather than a single order parameter for the entire system¹⁷. This results in rapid increase in atomic disorder as each unit cell undergoes a unique pathway to the high symmetry state. As a result, the order parameter cannot transiently cross-over to other domains during the phase transition, and once the order is lost, it remains lost. Therefore, determining which systems show disorder transitions and how the transient properties emerge is crucial for understanding transient phases in correlated materials.

It remains an open question whether TDGL can describe such order-disorder transitions. In principle, the individual trajectories of the underlying atomic system result in dephasing on a coarse-scale, which can be incorporated in the TDGL as an overdamped response. In this case, the order parameter maps the coarse-grained mean response of the system. However, the mean dynamic does not have to act as a reliable measure for the local dynamics in the system. TDGL in particular, and mean-field theories more generally, assume that the local distribution of the order parameters is compact around the mean value¹⁸, even when spatial inhomogeneity is included^{19,20}. This assumption can break down if the transition is heterogeneous, which is typical in 1st order phase transitions. Figure 1 shows a spatially resolved order parameter for two pump-induced order-disorder scenarios where the mean order parameter is reduced by 50%. In one case, the system follows TDGL theory and the order parameter can take any value, even down to the atomic scale, and thus the distribution of local order parameter values is centred at 50%. Alternatively, a system could completely switch locally in 50% of the sample. Here the distribution is bi-modal, and no part of the system is actually in the state suggested by the mean. This distinction is particularly important because, if materials with first-order transitions in equilibrium exhibit dynamics governed by second-order like TDGL, the order parameter can be manipulated non-thermally, whereas if first-order transitions cannot be described by TDGL, new theory beyond mean-field is needed to truly understand the transient properties of these materials.

In this paper, we present direct measurements of the order parameter dynamics in the C₄-symmetry restoring phase-transition of the prototypical quasi-2D single layer manganite La_{0.5}Sr_{1.5}MnO₄ (LSMO) following ultrafast photoexcitation through ultrafast optical anisotropy. We chose this compound because the equilibrium properties have been extensively studied and the phase transition is first order^{21,22}. Furthermore, the C₄ symmetry breaking dynamics in the related compound Pr_{0.5}Ca_{1.5}MnO₄ have been described in terms of TDGL theory, and manganites in general have been found to host a variety of emergent transient and metastable light-induced phases. We find that, while the order parameter dynamics qualitatively resemble those of an overdamped Ginzburg-Landau response, this similarity breaks down upon closer examination. Most strikingly, we find that the time-scale for the phase transition decreases with fluence, and that a global change in the lattice potential occurs within 25 fs. The picture that emerges is one in which all accessible degrees of freedom are excited by the laser leading to rapid disorder and points towards physics beyond the mean field approximation. Our results

imply that all first-order phase transitions could respond in this way, but the process can be masked by initial state inhomogeneity. As inhomogeneity is common in first-order transitions, and is often invoked to explain pump probe data^{23,24}, these results will impact a broad range of light induced transitions.

Results

LSMO undergoes a first order insulator-to-semiconductor phase transition at $T_{CO} \approx 230$ K, referred to as charge and orbital ordering. The phase transition involves the condensation of multiple phonon modes, primarily of oxygen character, which break the equivalence (charge ordering, CO) and isotropy (orbital ordering, OO) of the Mn environment, changing the space group from $I4/mmm$ to $Cmnm$ and quadrupling the unit cell²¹. To date, most probes of the order parameter have focused on diffraction, however the reduction to C_2 symmetry also results in electronic anisotropy and optical birefringence^{8,25,26}. Two coefficients r_1 and r_2 , the reflectivity parallel and perpendicular to the anisotropy axis, fully describe the ab -plane reflection anisotropy (RA). The anisotropy axis can lie along either the $[110]$ or $[1-10]$ directions of the crystal, resulting in multiple four possible domain configurations, as depicted in Figure 2a. Just as with X-rays, optics can only distinguish two sets because the anisotropy is only sensitive to the square of the order parameter (see Supplementary Information S3). Domains situated in opposite quadrants of the phase diagram are connected by a 180° rotation and lattice translation, and are thus optically identical, whereas domains in adjacent quadrants are related by 90° rotations and have opposite optical anisotropies. The normalized order parameter, $\eta^2 = 2 \frac{r_1 - r_2}{r_1 + r_2}$, and the isotropic reflectivity $r = \frac{r_1 + r_2}{2}$ can thus be determined by measuring the polarization-dependent reflectivity (see Methods for details).

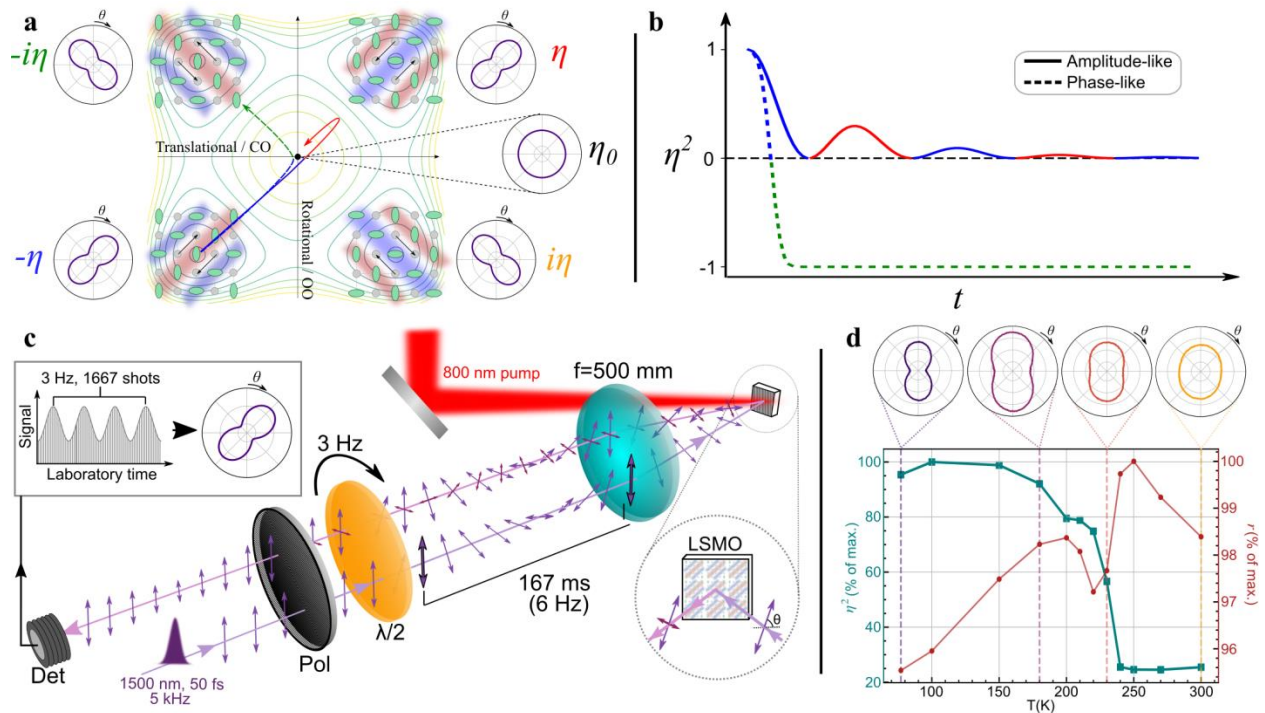


Figure 2. C_4 symmetry breaking and reflection anisotropy in $\text{La}_{0.5}\text{Sr}_{1.5}\text{MnO}_4$. **a** Schematic representation of the potential energy surface of the symmetry broken phase. The four minima ($\pm\eta$, $\pm i\eta$) correspond to the directions along which the low temperature phase can form, relative to the high symmetry structure, labelled η_0 . Inserts show the reflection anisotropy signal for each domain structure, which can

point along the [110] or [1-10] crystallographic axis. Domains of opposite parity have the same anisotropy and are thus indistinguishable. **b.** Expected signals for η^2 based on the two pathways shown in **a.** An amplitude-mode-like motion, in which the order is restored along a direct pathway, but overshoots, resulting in a “rebound” in the signal, and a phase-like motion, which flips the anisotropy axis (Line colour corresponds to the domain state). **c** Experimental setup for measurement of time-dependent anisotropy. A 60 fs 1500 nm probe pulse passes through a linear polarizer and rotating a halfwave plate. The probe is focused onto the LSMO sample, where the polarization component parallel to the input state is attenuated and a transverse component with a complex phase delay is introduced. The reflected beam is collected by the same lens and propagates back through the waveplate, where the initial polarization rotation is undone. The beam then passes back through the linear polarizer, removing the transverse polarization component introduced by the LSMO, and the modulated parallel component is collected on a photodiode. The real time-modulation of the signal is processed to yield the angular anisotropy signal (inset, top left). **d** η^2 and r as a function of temperature in our single-crystal LSMO sample. The polar plot radial axes run from 1.42 to 1.8 with divisions marked every 0.1 (arb. units). η^2 shows a clear discontinuity at T_{co} while r is less sensitive. The small non-zero value of η^2 above T_{co} is due to strain.

Measuring the full reflection anisotropy (RA) pattern in the time domain can give a direct measurement of the order parameter dynamics following photoexcitation, in particular any coherent evolution. Figure 2b shows the evolution of η^2 expected for two such melting transitions. In the first case, an amplitude-mode-like transition (blue/red), the system moves directly to the high-symmetry D0 state but, due to its momentum, continues to the opposite domain. The anisotropy drops to zero as the system passes through the D0 state and then “rebounds” as the system overshoots due to the indistinguishable nature of the domains. Similar rebounds in the order parameter are frequently claimed in the dynamics of X-ray diffraction peaks of many systems^{10,12,14}. Alternatively, domain rotation could occur (blue/green). In this case, the system again shows an anisotropy decrease as the system reaches D0, before re-emerging with the opposite phase, i.e. the anisotropy signal switches sign.

To probe the dynamics we built a high-speed RA setup (Figure 2c) that is compatible with ultrafast laser pulses. A high-speed spinning waveplate is used to modulate the polarization state of the laser shot-to-shot, enabling us to measure a full reflection anisotropy pattern in ~ 170 ms of acquisition and with 80 femtosecond time resolution (see methods for further details). The temperature dependence of r and η^2 measured with our RA setup is shown in Figure 2d. The isotropic part of the reflectivity is temperature dependent, but has no clear marker for T_{co} , whereas the anisotropic component is small and constant above T_{co} , and dramatically increases in magnitude as the sample is cooled below T_{co} and C_4 symmetry is broken.

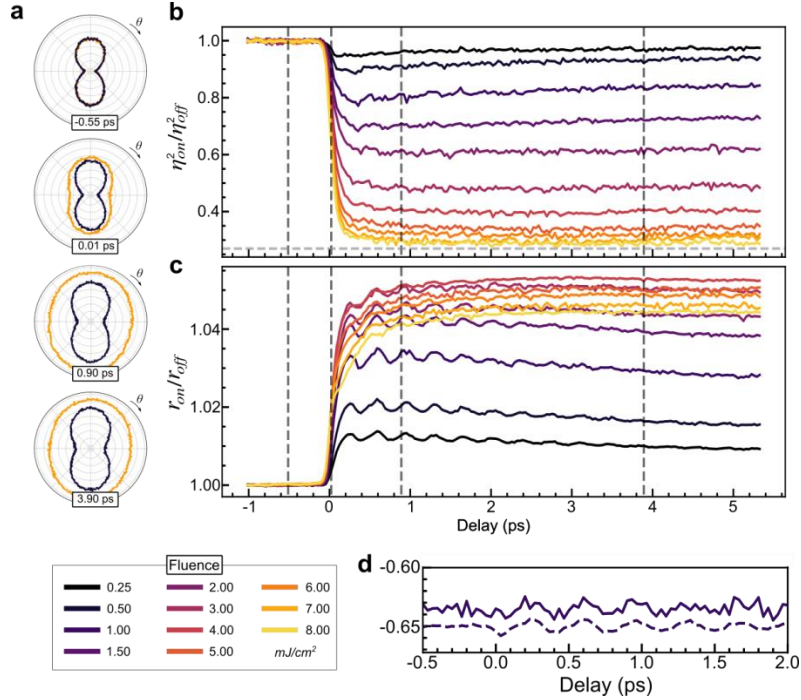


Figure 3. Time dependent reflection anisotropy measurements of LSMO during the photoinduced phase transition. **a** RA patterns as a function of pump-probe time delay for high (orange) and low (black) fluence. The radial axis runs from 1.63 to 2.015, with divisions every 0.05 (arb. units). **b** Ultrafast evolution of the normalized order parameter η^2 as a function of pump fluence which shows an ultrafast suppression. **c** Ultrafast evolution of the isotropic reflectivity r , showing a coherent phonon oscillations at 2.7 THz. **d** comparison of η^2 and r at 0.5 mJ/cm^2 showing the 2.7 THz mode weakly modulates the RA signal. Supplementary Video 1 and Supplementary Video 2 show the RA pattern of each time delay for pump fluences of 1.5 and 8 mJ/cm^2 , respectively, together with the corresponding plots of r and η^2 .

In Figure 3a, we show the restoration of C_4 symmetry in LSMO at 180 K after excitation with an 800 nm pump pulse. The RA pattern at several delays when the C_4 symmetry is partly (black) and completely (orange) recovered. The isotropic reflectivity notably increases while the order parameter decreases; see Supplementary Videos 1 and 2. At this temperature, high fluences can restore the C_4 symmetry without accumulative heating effects. At lower temperatures, high fluences could generate a metastable state, as found in other manganites²⁷⁻²⁹, making the results there unreliable.

To get quantitative insight into the dynamics, we plot the time dependence of η^2 and r for several fluences in Figure 3b and c. At low fluences the isotropic reflectivity shows a fast increase and large amplitude coherent oscillations at 2.7 THz, followed by a slow exponential decay. However, at higher fluences the initial jump is suppressed and a slow rise is seen, together with a suppression of the phonon signal. These isotropic dynamics bear little resemblance to the response of the order parameter, which shows a rapid and incoherent suppression. As the fluence is increased, the order parameter suppressed to a greater degree and eventually saturates at the strain level observed above T_{co} . While it is clear that a coherent TDGL theory cannot explain this data, an overdamped TDGL response may still be applicable. Indeed, the fluence dependence of the order parameter (Figure 4a) shows a continuous decrease with fluence and no evidence of a threshold, consistent with the thresholdless response expected from TDGL. Therefore, intermediate values of the order parameter in LSMO could be

interpreted as a transient non-thermal structure and indicate that the overdamped response of LSMO is fundamentally different from VO₂, despite both systems showing first-order transitions in equilibrium.

However, according to TDGL theory, the order-parameter dynamics should slow down the closer the system gets to complete melting of the phase transition. In direct contrast, the normalized response of the order parameter shown in Figure 4b shows that the order parameter actually speeds up as the system approaches the phase transition. We note that the reflectivity dynamics (Figure 4c) do slow down when pumped across the phase transition, as has been interpreted as a signature of critical slowdown¹¹ or a bottle-neck timescale^{2,26,30} in other materials, but here is found to be unrelated to the order parameter. Notably the isotropic reflectivity shows significant probe wavelength dependence, while the anisotropic dynamics do not (Supplementary Figure S4), indicating the reflectivity measures dynamics of different degrees of freedom.

To better understand the transient state, we examine the response of the lattice through the coherent phonons. The 2.7 THz mode, which modulates the reflectivity, has a weak effect on the order parameter (Figure 3d). It is known from Raman measurements that this mode is not the amplitude mode of the transition, but rather represents motion of the La/Sr ions^{15,31} which play no role in the transition in equilibrium. The slight modulation seen then implies that either the phonon weakly drives the order parameter, or the mode itself generates an additional anisotropy independent of the order parameter, similar to strain. However, the concomitant loss in phonon signal with the suppression of the order parameter suggests an intimate connection between both degrees of freedom at the phase transition despite their weak coupling.

Due to the quadrupling of the unit cell during the phase transition, multiple phonon modes, that are otherwise forbidden in the high symmetry state, become Raman active in the low temperature phase and thus can potentially be excited by the laser. While the 2.7 THz mode does not play an active role in the phase transition, high-frequency Jahn-Teller modes have been suggested as being responsible for the transition³². To access these modes, we use sub-15 fs resolution transient reflectivity measurements (see methods). Figure 4d shows that 2.7, 6, 16 and 19 THz modes can all be observed at low fluence, consistent with equilibrium Raman scattering data³³. Importantly, all modes show changes when the order parameter is suppressed, with the 2.7 and 6 THz modes also becoming suppressed and the 16 and 19 THz modes broadened into a single peak. The concomitant changes suggest the entire potential for all degrees of freedom is perturbed, and not just a subset directly connected to the order parameter as assumed in TDGL. This change must be occurring faster than the highest frequency mode we measure, suggesting a sub-25 fs timescale. The excitation of a large number of modes then describes an order-disorder transition.

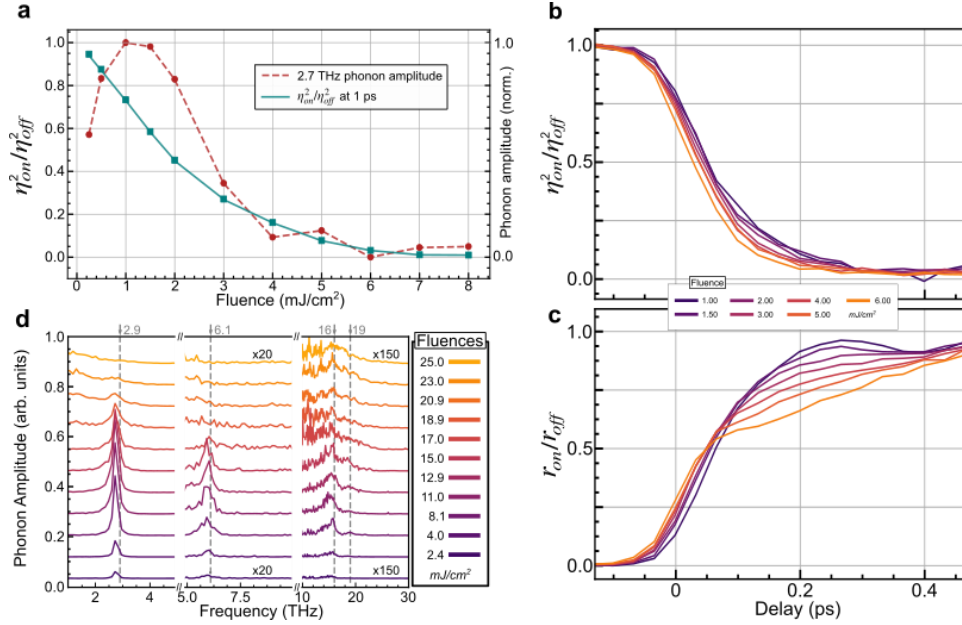


Figure 4. Simultaneous excitation of multiple degrees of freedom in LSMO. **a** Fluence dependence of the order parameter and the amplitude of the 2.7 THz mode from r . The order-parameter shows a monotonic decrease whereas the phonon amplitude first rises before being suppression at the same fluences as the order parameter. **b** Focused and normalized view of the first 500 fs of η^2 showing a marked speedup with increasing fluence. **c** Same as **b** but for r . In contrast to η^2 a slowdown is observed with increasing fluence. **c** Few-cycle pump probe measurements of phonon dynamics with 1800 nm pump and 650 nm probe pulses (see methods and Supplementary Figure S5 for details). 2.7 THz, 6 THz, 16 THz and 19 THz modes of LSMO are clearly observed and in good agreement with the literature³³ (dashed lines). The 2.7 THz and 6 THz modes are suppressed as the system is pumped through the transition, while the high frequency modes broaden.

To understand how to interpret our data beyond TDGL, we investigate the role of inhomogeneity in the system. In first order phase transitions inhomogeneity is known to locally modify the critical temperature, and in LSMO in particular, it is known that the orbital ordering melts at the surface before the bulk³⁴. As our probe is absorbed in less than the first 100 nm¹⁵, we are sensitive to this effect and it, together with other sources of inhomogeneity, results in the smooth thermal transition experimentally observed in Figure 2d. Importantly, the continued increase in orbital order below T_{co} is not due to an increasing magnitude of a local order, as would be the case for a homogeneous second order transition, but results from more of the sample becoming ordered. We note that a coherent but inhomogeneous transition should still show coherent signatures in the order parameter¹⁵, thus the order-disorder result is independent of this contribution.

This can have a major influence on understanding the fluence dependence, as shown in Figure 5. Close to T_{oo} , results in pre-melting of the orbital surface. Any energy absorbed by the laser can then move the ordered surface deeper into the bulk and there is no threshold to melt the surface of the system, even if a critical fluence dependence would be observed in a homogenous system. The system completely melts once the ordered surface has been pushed deep into the bulk and out of the probed volume (Figure 5b). Thus, the threshold-less behaviour earlier taken as evidence of a 2nd-order-like TDGL can be explained without invoking a different order for the phase transition in- and out-of-equilibrium. By repeating our measurements at 1200 nm, which penetrates less deeply than 1500 nm, we confirm the critical role of inhomogeneity in the system (Figure 5d). While this fluence dependence can be described within TDGL

theory, if the critical exponent is allowed to be different from the thermodynamic value, our approach does not need to consider such a change in behaviour. (see Supplementary Information S7 for a more detailed discussion on fluence dependence within TDGL). A discrete, 1st-order-like switching also explains the lack of softening seen in the Raman modes as only the regions which are ordered oscillate, while those that are disordered cannot.

Discussion

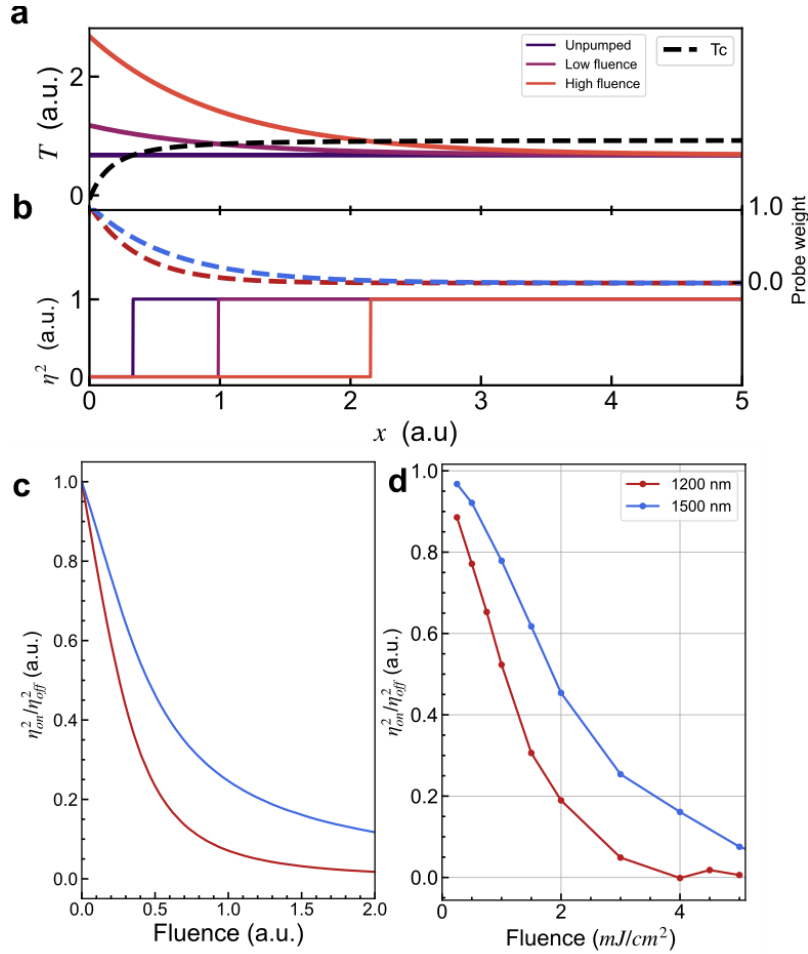


Figure 5. Inhomogeneity in the photo induced phase transition. **a** First order phase transitions can show surface melting, with the orbital of the phase transition melting at a lower transition temperature than the bulk. The black dashed line shows the thermodynamic transition temperature as a function of position in the sample from the surface at $x=0$, together with two pump-induced temperature profiles. **b** The effect of the pump on the spatial dependence of the order parameter. Due to surface melting, part of the sample is already melted before the pump, resulting in a phase front. This phase front moves deeper into the bulk for harder excitation. The dashed lines indicate the weighting of the local order parameter on the averaged order parameter measured by probes which penetrate two different depths. **c** The measured order parameter as a function of pump fluence for two different probe conditions. Probes that penetrate less into the bulk reach saturation at a lower fluence than those that penetrate deeper. **d** Experimental data showing that changing the probe wavelength to 1200 nm reaches saturation before 1500 nm, demonstrating the role of spatial inhomogeneity in the probe.

Our results show that photoexcited LSMO undergoes an inhomogeneous and local ultrafast disordering, where all degrees of freedom are excited simultaneously and not just those required for the phase transition. The resulting dynamics then take place in a multi-dimensional phase space and when the system is more strongly excited, more phase space becomes accessible enabling the system to disorder faster. Such an effective change in dimensionality seems to be almost instantaneous, with the lattice responding to the change in symmetry in less than one-half period of the high frequency mode (25 fs). This points to physics beyond TDGL, which is a low dimensional theory in which the system is necessarily coarse-grained and the main dynamics are confined to the order parameter in a restricted phase space of the global system. The close proximity to a metastable state in our sample also suggests a shared disorder origin for metastable states observed across the manganites^{27,29}.

While only VO₂ and LSMO have been described in terms of order-disorder transitions to date, the local dynamics which characterize 1st order phase transitions in equilibrium naturally lend themselves to inhomogeneous, disordered transitions. In spite of this, many transient phase changes in first order materials, such as charge density wave systems, have been modelled with TDGL. It then remains an open question as to if and why some C₄-symmetric systems should a fundamentally non-thermal and coherent response while others show disorder. Key to resolving this issue will be to understand how inhomogeneity both before³⁵ and after excitation could impact interpretations based on TDGL theory. To this end, the need for techniques that can image the initial inhomogeneity as well as their dynamics^{36,37} will be increasingly important³⁸⁻⁴¹. Alternatively, disorder and fluctuations may stabilize the equilibrium high temperature phase in both VO₂⁴² and LSMO²² as both systems show large fluctuations above T_c, and systems that are stabilized by entropy may show fundamentally different dynamics to those driven by soft modes.

Disordered states in quantum materials in equilibrium are emerging as a new route to explain and generate new phenomena⁴³. To date, explanations of effects such as light-induced superconductivity, have focused on possible non-equilibrium, ordered transient crystal structures⁴⁴ that would be expected from TDGL approaches. However, these systems also show large amounts of light induced inhomogeneity and the restoration of C₄ symmetry would also be expected to generate disorder. Thus, our results hint that ultrafast disorder may in fact be responsible for the desirable properties in layered quantum materials.

Methods

Sample growth and characterization

A single crystal of LSMO was grown using the optical float-zone method and cut with a 001 surface, then polished to an optical finish. All measurements presented here were performed on the same crystal. The transition was characterized using the temperature-dependent magnetisation, which shows a single peak at T_{co} in agreement with the RA measurements. Samples from the same batch were characterized by X-ray diffraction for their charge and magnetic order peaks.

Reflection anisotropy setup

The reflection anisotropy was measured with linearly polarized 1500 nm pulses of 60 fs duration at 5 kHz repetition rate. A halfwave plate rotating at 3 Hz was used to probe the sample with all the possible linear polarization angles. For the time resolved experiment, 800 nm pump pulses of 50 fs duration at 5 kHz repetition rate were used. An important aspect of our setup is that the polarization state on the

majority of optical elements is constant, enabling precise measurements of the RA signal. The LSMO sample was held in an open cycle nitrogen cryostat. Some inhomogeneity in the RA signal as a function of the position on the sample was observed, and so the probing position was kept constant by correcting any thermal dilation effects. More details can be found in Supplementary Information S1-S6.

High time resolution setup

High-frequency phonon dynamics were studied using 1800 nm pump pulses of 11 fs duration and 650 nm probe pulses of 10 fs duration at 1 kHz repetition rate. A time resolution of 25 fs, sufficient for observing the fastest phonon modes in LSMO, was determined from their cross correlation in a fifteen micron thick BBO crystal (Supplementary Figure S2). Further details of these sources can be found in A.S. Johnson *et al.*⁴⁵ and Amuah, E.B *et al.*⁴⁶. An achromatic ultrafast spectroscopy system compatible with few-cycle duration pulses was used to perform the pump-probe measurements at near-normal incidence. The LSMO sample was held in a closed cycle helium cryostat at 180 K, and pump-induced changes to the probe reflectivity were recorded with a pair of diodes sampling the parallel and perpendicular polarization components. The traces in Figure 4 average over polarization dependent effects. The pump spot size was set to ≈ 50 times larger than the probe to ensure homogenous excitation, and the pump beam was chopped at 250 Hz.

Fluence dependence model

We use a simple 1D model of the LSMO order parameter (OP) in which the critical temperature varies according to a power law from the surface. Regions with a temperature higher than the critical temperature have OP=0, while those below have OP=1; the probe beam samples an exponentially decaying region of the sample according to the wavelength, and we integrate this sampling to return the effective OP observed. The critical temperature curve was adjusted to approximate the thermal first-order transition observed. Optical pumping was modelled as an exponentially decaying additive temperature, see Supplementary Information S7 for more information.

Data Availability

The authors declare that all data supporting the findings of this study are available within the paper and its supplementary information files

References

1. Fiebig, M., Miyano, K., Tomioka, Y. & Tokura, Y. Visualization of the local insulator-metal transition in $\text{Pr}_{0.7}\text{Ca}_{0.3}\text{MnO}_3$. *Science* **280**, 1925–1928 (1998).
2. Polli, D. *et al.* Coherent orbital waves in the photo-induced insulator-metal dynamics of a magnetoresistive manganite. *Nat. Mater.* **6**, 643–7 (2007).
3. Miyano, K., Tanaka, T., Tomioka, Y. & Tokura, Y. Photoinduced insulator-to-metal transition in a perovskite Manganite. *Phys. Rev. Lett.* **78**, 4257–4260 (1997).
4. Nicoletti, D. *et al.* Optically induced superconductivity in striped $\text{La}_{2-x}\text{Ba}_x\text{CuO}_4$ by polarization-selective excitation in the near infrared. *Phys. Rev. B* **90**, 100503(R) (2014).
5. Khanna, V. *et al.* Restoring interlayer Josephson coupling in $\text{La}_{1.885}\text{Ba}_{0.115}\text{CuO}$ by charge transfer melting of stripe order. *Phys. Rev. B* **93**, 224522 (2016).

6. Basov, D.N., Averitt, R.D. & Hsieh, D. Towards properties on demand in quantum materials. *Nat. Mater.* **16**, 1077–1088 (2017).
7. Ogasawara, T., Kimura, T., Ishikawa, T., Kuwata-Gonokami, M. & Yokura, Y. Lattice symmetry breaking in cuprate superconductors: Stripes, nematics, and superconductivity. *Adv. Phys.* **58**, 699–820 (2009).
8. Ogasawara, T. *et al.* Dynamics of photoinduced melting of charge/orbital order in a layered manganite $\text{La}_{0.5}\text{Sr}_{1.5}\text{MnO}_4$. *Phys. Rev. B* **63**, 113105 (2001).
9. Först, M. *et al.* Femtosecond x rays link melting of charge-density wave correlations and light-enhanced coherent transport in $\text{YBa}_2\text{Cu}_3\text{O}_{6.6}$. *Phys. Rev. B* **90**, 184514 (2014).
10. Trigo, M. *et al.* Coherent order parameter dynamics in SmTe_3 . *Phys. Rev. B* **99**, 104111 (2019).
11. Zong, A. *et al.* Dynamical Slowing-Down in an Ultrafast Photoinduced Phase Transition. *Phys. Rev. Lett.* **123**, 97601 (2019).
12. Huber, T. *et al.* Coherent structural dynamics of a prototypical charge-density-wave-to-metal transition. *Phys. Rev. Lett.* **113**, 026401 (2014).
13. Duan, S. *et al.* Optical manipulation of electronic dimensionality in a quantum material. *Nature* **595**, 239 (2021).
14. Neugebauer, M. J. *et al.* Optical control of vibrational coherence triggered by an ultrafast phase transition. *Phys. Rev. B* **99**, 220302 (2019).
15. Beaud, P. *et al.* A time-dependent order parameter for ultrafast photoinduced phase transitions. *Nat. Mater.* **13**, 923–927 (2014).
16. Maklar, J. *et al.* Nonequilibrium charge-density-wave order beyond the thermal limit. *Nat. Commun.* **12**, 2499 (2021).
17. Wall, S. *et al.* Ultrafast disordering of vanadium dimers in photoexcited VO_2 . *Science* **362**, 572–576 (2018).
18. Tröster, A., Dellago, C. & Schranz, W. Free energies of the 4 model from Wang-Landau simulations. *Phys. Rev. B* **72**, 094103 (2005).
19. Dolgirev, P.E., Michael, M.H., Zong, A., Gedik, N. & Demler, E. Self-similar dynamics of order parameter fluctuations in pump-probe experiments. *Phys. Rev. B* **101**, 174306 (2020).
20. Sun, A. & Millis, A.J. Transient trapping into metastable states in systems with competing orders. *Phys. Rev. X* **10**, 21028 (2019).
21. Herrero-Martin, J., Blasco, J., García, J., Subías, G. & Mazzoli, C. Structural changes at the semiconductor-insulator phase transition in the single-layered perovskite $\text{La}_{0.5}\text{Sr}_{1.5}\text{MnO}_4$. *Phys. Rev. B* **83**, 184101 (2011).
22. Laroche, S. *et al.* Structural and magnetic properties of the single-layer manganese oxide $\text{La}_{1-x}\text{Sr}_x\text{MnO}_4$. *Phys. Rev. B* **71**, 024435 (2005).
23. Abreu, E. *et al.* Dynamic conductivity scaling in photoexcited V_2O_3 thin films. *Phys. Rev. B* **92**, 085130 (2015)

24. Abreu, E. *et al.* Nucleation and growth bottleneck in the conductivity recovery dynamics of nickelate ultrathin films. *Nano Lett.* **20**, 7422 (2020)
25. Miller, T. A. *et al.* Terahertz field control of in-plane orbital order in $\text{La}_{0.5}\text{Sr}_{1.5}\text{MnO}_4$. *Nat. Commun.* **6**, 8175 (2015).
26. Singla, R. *et al.* Photoinduced melting of the orbital order in $\text{La}_{0.5}\text{Sr}_{1.5}\text{MnO}_4$ measured with 4-fs laser pulses. *Phys. Rev. B* **88**, 075107 (2013).
27. Teitelbaum, S. W. *et al.* Dynamics of a Persistent Insulator-to-Metal Transition in Strained Manganite Films. *Phys. Rev. Lett.* **123**, 267201 (2019).
28. Takubo, N., Onishi, I., Takubo, K., Mizokawa, T. & Miyano, K. Photoinduced metal-to-insulator transition in a manganite thin film. *Phys. Rev. Lett.* **101**, 177403 (2008).
29. Zhang, J. *et al.* Cooperative photoinduced metastable phase control in strained manganite films. *Nat. Mater.* **15**, 956–960 (2016).
30. Cavalleri, A., Dekorsy, Th., Chong, H.H.W., Kieffer, J.C. & Schoenlein, R.W. Evidence for a structurally-driven insulator-to-metal transition in VO_2 : A view from the ultrafast timescale. *Phys. Rev. B* **70**, 161102(R) (2004).
31. Amelitchev, V. A. *et al.* Structural and chemical analysis of colossal magnetoresistance manganites by Raman spectrometry. *Phys. Rev. B* **63**, 1044301 (2001).
32. Rettig, L. *et al.* Disentangling transient charge order from structural dynamics contributions during coherent atomic motion studied by ultrafast resonant x-ray diffraction. *Phys. Rev. B* **99**, 134302 (2019).
33. Yamamoto, K., Kimura, T., Ishikawa, T., Katsufuji, T. & Tokura, Y. Raman spectroscopy of the charge-orbital ordering in layered manganites. *Phys. Rev. B* **61**, 14706 (2000).
34. Wilkins, S. B. *et al.* Surface melting of electronic order in $\text{La}_{0.5}\text{Sr}_{1.5}\text{MnO}_4$. *Phys. Rev. B* **84**, 165103 (2011).
35. O'Calaghan, B.T. *et al.* Inhomogeneity of the ultrafast insulator-to-metal transition dynamics of VO_2 . *Nature Communications* **6**, 6849 (2015)
36. Vidas, L *et al.* Imaging Nanometer Phase Coexistence at Defects during the insulator-metal phase transformation in VO_2 Thin Films by Resonant Soft X-ray holography. *Nano Lett.* **18**, 3449-3453 (2018)
37. Johnson, A. S *et al.* Quantitative hyperspectral coherent diffractive imaging spectroscopy of a solid-state phase transition in vanadium dioxide. *Sci. Adv.* **7**, eabf1386 (2021)
38. Plankl, M *et al.* Subcycle contact-free nanoscopy of ultrafast interlayer transport in atomically thin heterostructures. *Nat. Photo* **15**, 594-600 (2021)
39. Dönges, S. A. *et al.* Ultrafast Nanoimaging of the Photoinduced Phase Transition Dynamics in VO_2 . *Nano Lett.* **16**, 3029-3035 (2016)
40. Danz, T., Domröse, T. & Ropers, C. Ultrafast nanoimaging of the order parameter in a structural phase transition. *Science* **371**, 371-374 (2021)
41. Sternbach, A. J. *et al.* Nanotextured Dynamics of a Light-Induced Phase Transition in VO_2 . *Nano*

Lett. **21**, 9052-9060 (2021)

42. Budai, J. D. *et al.* Metallization of vanadium dioxide driven by large phonon entropy. *Nature* **515**, 535–539 (2014).
43. Simonov, A. & Goodwin, A.L. Designing disorder into crystalline materials. *Nat. Rev. Chem.* **4**, 657–673 (2020).
44. Mankowsky, R. *et al.* Nonlinear lattice dynamics as a basis for enhanced superconductivity in $\text{YBa}_2\text{Cu}_3\text{O}_{6.5}$. *Nature* **516**, 71–73 (2014).
45. Johnson, A.S., Amuah, E.B., Brahms, C. & Wall, S. Measurement of 10 fs pulses across the entire Visible to Near-Infrared Spectral Range. *Sci. Rep.* **10**, 4690 (2020).
46. Amuah, E.B., Johnson, A.S. & Wall, S. An achromatic pump–probe setup for broadband, few-cycle ultrafast spectroscopy in quantum materials. *Review of Scientific Instruments* **92**, 103003 (2021).

Acknowledgements

We acknowledge insightful discussions with M. Eckstein. This work was funded through the European Research Council (ERC) under the European Union’s Horizon 2020 Research and Innovation Programme (Grant Agreement No. 758461), by the Ministry of Science, Innovation and Universities (MCIU), State Research Agency (AEI) and European Regional Development Fund (FEDER) PGC2018-097027-B-I00, the Spanish State Research Agency through the “Severo Ochoa” program for Centers of Excellence in R&D (CEX2019-000910-S), the Fundació Cellex, and Fundació Mir-Puig, the Generalitat de Catalunya through the CERCA program, and EPSRC (grant no. EP/H033939/1). A.S.J. acknowledges support from Marie Skłodowska-Curie grant agreement No. 754510 (PROBIST).

Author Contributions

D. PS designed and built the RA setup and performed the RA measurements assisted by A.S.J. A.S.J. designed and built the high temporal resolution setup and performed measurements together with D. PS. D.P grew and characterized the sample. S.W conceived of and organized the project. All authors participated in the writing of the manuscript.

Competing financial interests

The authors declare no competing financial interests.

Supplementary Information: Multi-mode excitation drives disorder during the ultrafast melting of a C4-symmetry-broken phase

Daniel Perez-Salinas^{1*}, Allan S. Johnson^{1*}, D. Prabhakaran², Simon Wall^{1,3}

¹ICFO – The Institute of Photonics Sciences, The Barcelona Institute of Science and Technology, 08860, Castelldefels, Barcelona, Spain

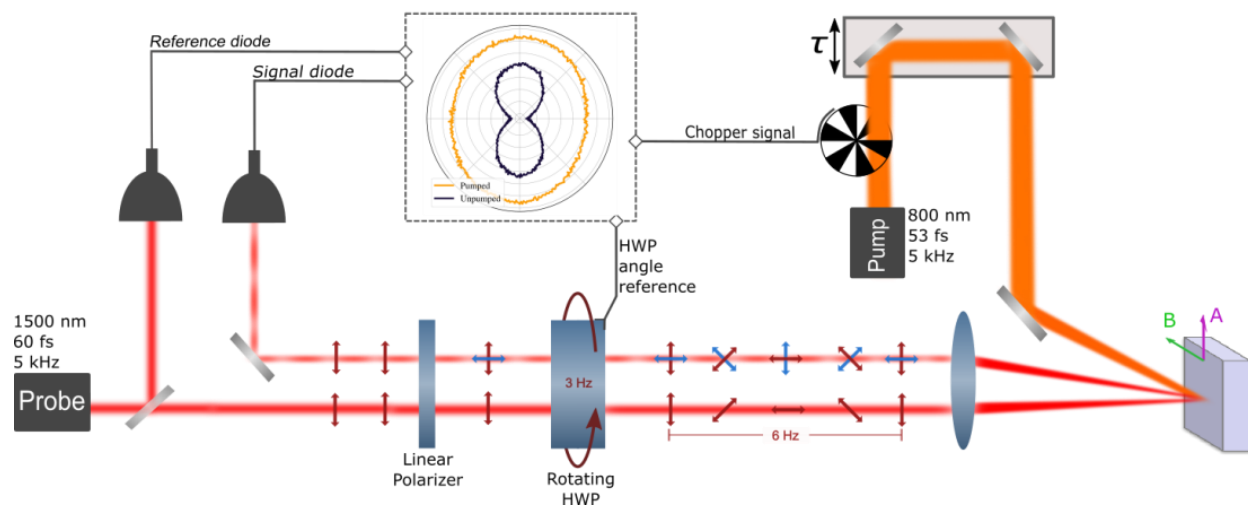
²Department of Physics, Clarendon Laboratory, University of Oxford, Oxford OX1 3PU, United Kingdom

³Department of Physics and Astronomy, Aarhus University, Ny Munkegade 120, 8000 Aarhus C, Denmark

*Equal contribution

Supplementary Methods

S1 Ultrafast reflection anisotropy setup



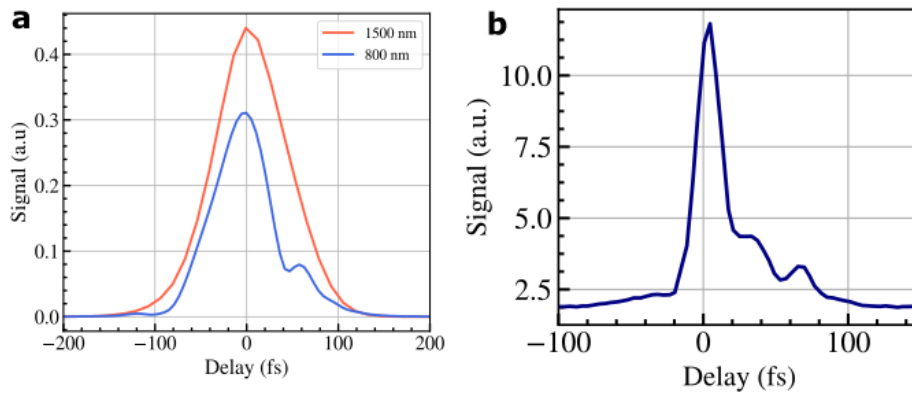
Supplementary Figure S1: Schematic of the reflection anisotropy setup. To measure the reflection anisotropy, we adopt a double-pass scheme using an optical parametric amplifier (OPA) operating at 5 kHz. A fraction of the output of the OPA is first sampled using a beam splitter and sent to a reference diode to normalize intensity fluctuations. The rest of the beam passes through a fixed wire-grid linear polarizer to define the polarization state, and then passes through a rotating waveplate (3Hz) which causes a rotation of the polarization by θ with respect to the initial polarization state. The beam is then focused onto the sample with a lens ($f = 500$ mm) though a 2 mm thick quartz cryostat window. The sample, mounted at near-normal incidence at the focal point of the lens, reflects the beam with a perturbed polarization state. The reflected beam passes back through the wave plate, causing the polarization to rotate by $-\theta$, undoing the initial rotation up to factor introduced by the sample (the rotation of the waveplate during the time taken to reflect from the sample is negligible). Finally, the light

passes through the initial polarizer, transmitting only the component parallel to the incident light. The transmitted component is collected with an InGaAs photodiode. The duration of the probe beam, measured at the sample plane using frequency resolved optical gating, was approximately 60 fs (Supplementary Figure S2), and the focal spot diameter was 150 μm .

The sample was excited with an 800 nm pump pulse from the same laser, mechanically delayed with respect to the probe pulses, and modulated with an optical chopper at 2.5 kHz. The polarization was approximately aligned to the low reflectivity principal axis and the pulse duration was 50 fs (Supplementary Figure S2). The pump spot size at the sample was approximately 7.5 times that of the probe.

The sample and reference diodes were read by a four-channel oscilloscope along with the angle of the rotation stage and the chopper state on a shot-by-shot basis. The data was then filtered by angle and chopper state into separate on and off channels. As the rotation stage was not synchronized to the laser, the accuracy of the waveplate position is 0.5 degrees. Static measurements are performed in the same way, but the chopper signal is discarded.

S2 Pulse duration measurements



Supplementary Figure S2: Pump and probe pulse durations. **a** Pump and probe pulses used in the reflection anisotropy setup reconstructed using frequency-resolved optical gating¹. The 800 nm pulses are of 50 fs duration (full-width half maximum) and the 1500 nm probe pulses are 60 fs duration. **b** Cross correlation of the 1800 nm pump and 650 nm probe pulses used in the high time resolution setup, measured in a 15 μm thick barium borate crystal. A full-width half maximum of 25 fs is obtained.

S3 Reflectivity of an anisotropic sample

We define the ab plane reflection coefficient as

$$R = \begin{pmatrix} r_1 e^{i\phi_1} & 0 \\ 0 & r_2 e^{i\phi_2} \end{pmatrix} = \alpha \begin{pmatrix} 1 & 0 \\ 0 & \rho e^{i\chi} \end{pmatrix},$$

where $\alpha = r_1 e^{i\phi_1}$, $\rho = \frac{r_2}{r_1}$, $\chi = \phi_2 - \phi_1$. For an arbitrary polarization state the reflectivity can be written as

$$R = \alpha \begin{pmatrix} \cos^2 \theta + \rho e^{i\chi} \sin^2 \theta & \frac{1}{2} \sin 2\theta (1 - \rho e^{i\chi}) \\ \frac{1}{2} \sin 2\theta (1 - \rho e^{i\chi}) & \sin^2 \theta + \rho e^{i\chi} \cos^2 \theta \end{pmatrix},$$

where θ is the angle made by the polarization relative to the crystal axis. Defining the input polarization as $\begin{pmatrix} 1 \\ 0 \end{pmatrix}$ and measuring the reflected parallel component, the detected intensity varies as

$$\begin{aligned} I_{VV} &= \frac{r_1^2}{8} (4(1 - \rho^2) \cos 2\theta + (1 + \rho^2 - 2\rho \cos \chi) \cos 4\theta + 6 + 2\rho \cos \chi) \\ &= I_{DC} + I_4 \cos 4\Phi + I_8 \cos 8\Phi. \end{aligned}$$

Here $\Phi = \frac{\theta}{2}$ is the angle of the waveplate, which rotates the polarization at twice the rate of the waveplate rotation. I_{DC} , I_4 and I_8 can be directly extracted from our data. All terms are sensitive to the birefringence ratio ρ , and thus the order parameter, as well as other factors.

We are unable to detect an eight-fold peak in our data; thus by setting $I_8 = 0$ we have $I_{DC} = \frac{r_1^2}{8} (7 + \rho^2)$ and $I_4 = \frac{r_1^2}{2} (1 - \rho^2)$. This allows us to solve for r_1 and ρ :

$$\begin{aligned} r_1^2 &= I_{DC} + \frac{I_4}{4}, \\ \rho^2 &= \frac{4 - 7 \frac{I_4}{I_{DC}}}{\left(4 + \frac{I_4}{I_{DC}}\right)}. \end{aligned}$$

When the system is isotropic, $I_4 = 0$, which implies $\rho = 1$. Values of $\rho > 1$ correspond to domains of one parity, whereas $\rho < 1$ corresponds to domains of the alternative parity. Optical measurements cannot distinguish between domains of the same parity, therefore $\eta^2 \propto r_1 - r_2$.

We normalize η^2 to lie in the range ± 1 with

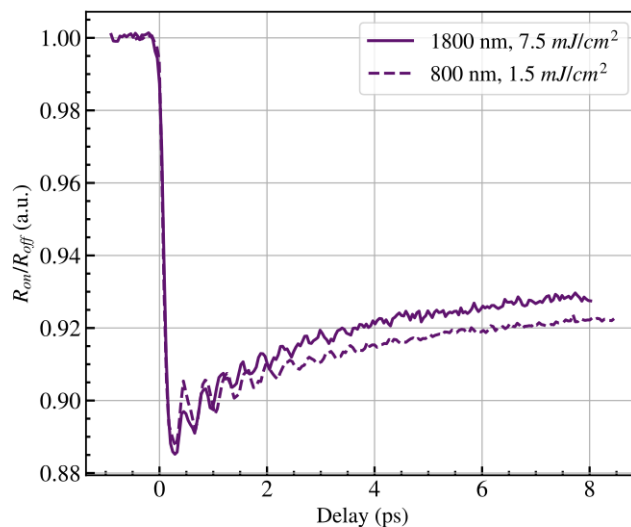
$$\eta^2 = 2 \frac{r_1 - r_2}{r_1 + r_2} = \frac{1 - \rho}{1 + \rho}.$$

When fitting the data, we fit as a function of the waveplate angle using the following equation for I_{VV} :

$$I_{VV}^f = I_{DC} + I_2 \cos(\theta + \psi_2) + I_4 \cos(2\theta + \psi_4).$$

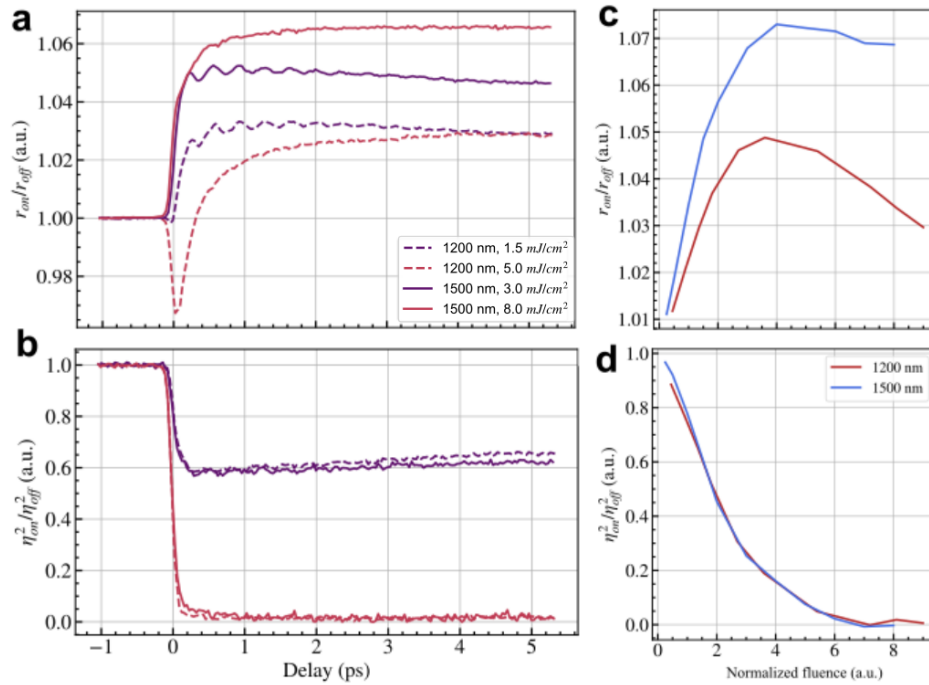
The I_2 term captures a small constant which is modulated at the frequency of the rotating waveplate. Such a term most likely corresponds to scatter from the waveplate to the detector. In addition, the phase term ψ_4 allows us to correct for the fact that the crystal axis are not perfectly aligned to the polarization axis. It also allows us to observe the direction of strain, which is not confined along a particular direction.

S4 Pump colour comparison



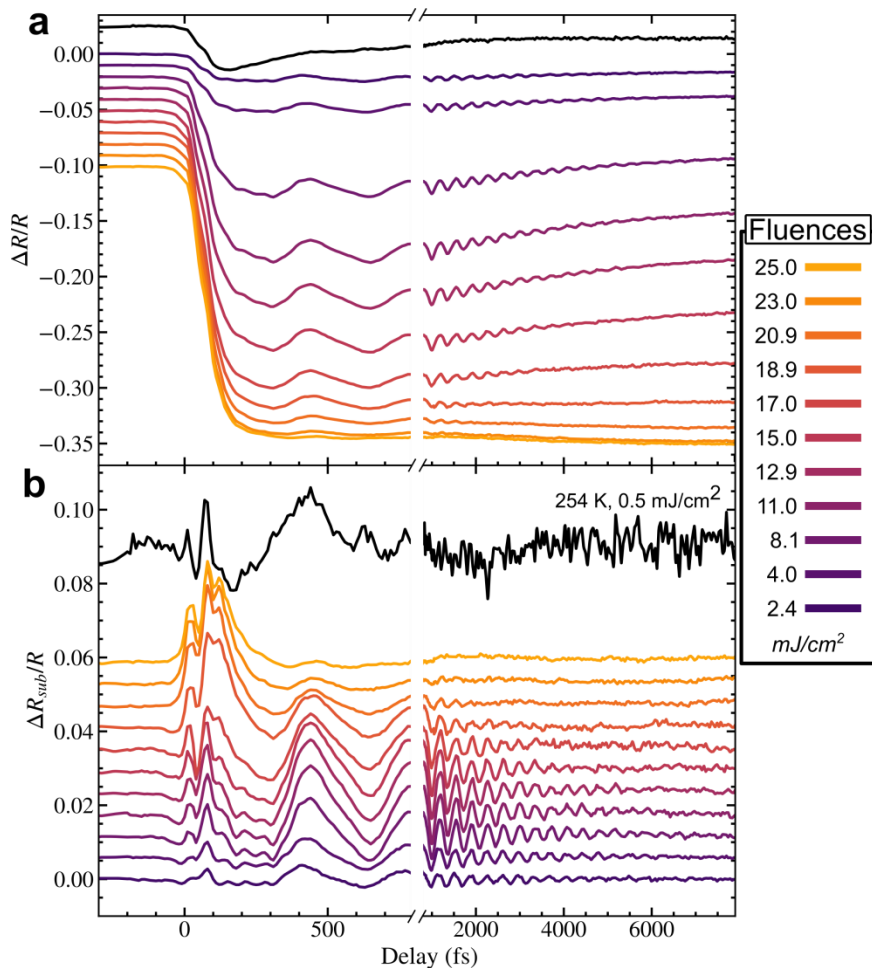
Supplementary Figure S3: Comparison of different pump wavelengths. Ultrafast reflection anisotropy measurements (as shown in Figure 2 and Figure 3a and b) were taken with 800 nm pump pulses, in contrast with the 1800 nm excitation used in the high time resolution setup (as shown in Figure 4c). To ensure the consistency of these two data sets we directly compare transient reflectivity dynamics measured with 800 nm and 1800 nm pump pulses in the high time resolution setup under identical probing condition. No appreciable differences are found, confirming the validity of the comparison.

S5 Probe colour comparison



Supplementary Figure S4: Probe wavelength dependence of the ultrafast evolution of the isotropic and anisotropic reflectivity of LSMO. **a** Ultrafast evolution of the isotropic reflectivity r and **b** normalized order parameter η^2 probed with 1500 nm (continuous lines) and 1200 nm (dashed lines) pulses. The baseline non-zero value for η^2 induced by strain has been compensated through renormalization for both probe colors. Dynamics of the r parameter show strong wavelength dependence, however this variation is absent in the order parameter dynamics. **c** and **d** show the fluence dependence of the 1 ps delay value of r and η^2 , respectively. The fluence axis for the 1200 nm data has been multiplied by 1.8 to account for the different penetration depths for the two probe colors, see following section.

S6 High temporal resolution data



Supplementary Figure S5: Few-cycle 1800 nm Pump, 650 nm probe transient reflectivity data. Fluence dependent data (coloured) is performed at 140 K, well below T_{co} , while the black trace ($T = 254$ K, 0.5 mJ cm⁻²) is performed above T_{co} . **a** Raw transient reflectivity changes (offset for clarity) and **b** background subtracted changes after fitting the data with multiple exponential decays. Measurements were performed at a near-normal angle of incidence as described in the methods section. Due to the different base temperatures and pump wavelengths, the fluences here are not directly comparable to the fluences used in the reflection anisotropy measurements in which the pump wavelength was 800 nm. With the exception of the absolute value of the threshold fluence, there was no significant difference in the dynamics with different pump wavelength (Supplementary Figure S3). At 140 K, we found that the sample could often, but not always, be switched to a meta-stable state with high fluence excitation. This results in a response that has different dynamics to the pristine state. Repeat measurements were performed to ensure that no meta-stable state was created in this case.

Supplementary Discussion

S7 Fluence dependence of the phase transition

We start by defining the local order parameter as the value of the order parameter at smallest valid length scale. For a dimerization transition, for example, this would be the degree of dimerization of the low temperature unit cell.

An initially inhomogeneous 1st order phase transition

As LSMO exhibits a first order phase transition with surface melting, we first model the phase transition in which the local T_c is reduced as the surface is approached as

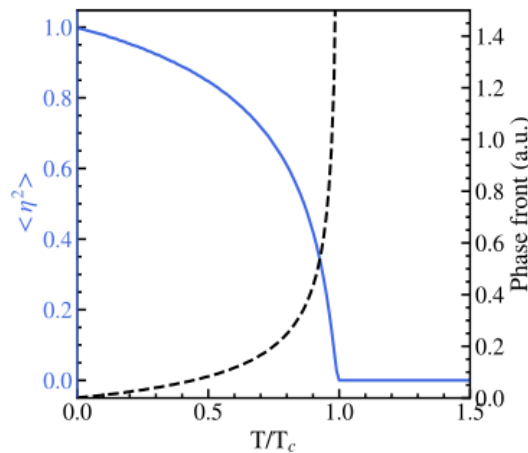
$$T_c(x) = T_B \left(1 - \frac{1}{(1 + ax)^2}\right)$$

Where $x=0$ corresponds to the surface of the crystal, and a is a constant that determines the thickness of the surface layer and T_B is the transition temperature of the bulk. We assume regions of the sample in which the temperature is below the local T_c are fully ordered ($\eta^2 = 1$), whereas the regions that are above the local T_c have no order ($\eta^2 = 0$). As a function of temperature, the system first starts to melt at the surface, with the ordered surface moving deeper into the bulk until all of the solid is transformed.

The probe light averages over a large length scale, penetrating exponentially into the material over a lengthscale l_{probe} . We assume that the measured order parameter is proportional to the intensity weighted average, i.e.

$$\langle \eta^2 \rangle = \frac{\int \eta^2(x) e^{-\frac{x}{l_{probe}}} dx}{\int e^{-\frac{x}{l_{probe}}} dx}$$

The average order parameter observed is shown in **Fig S6**.

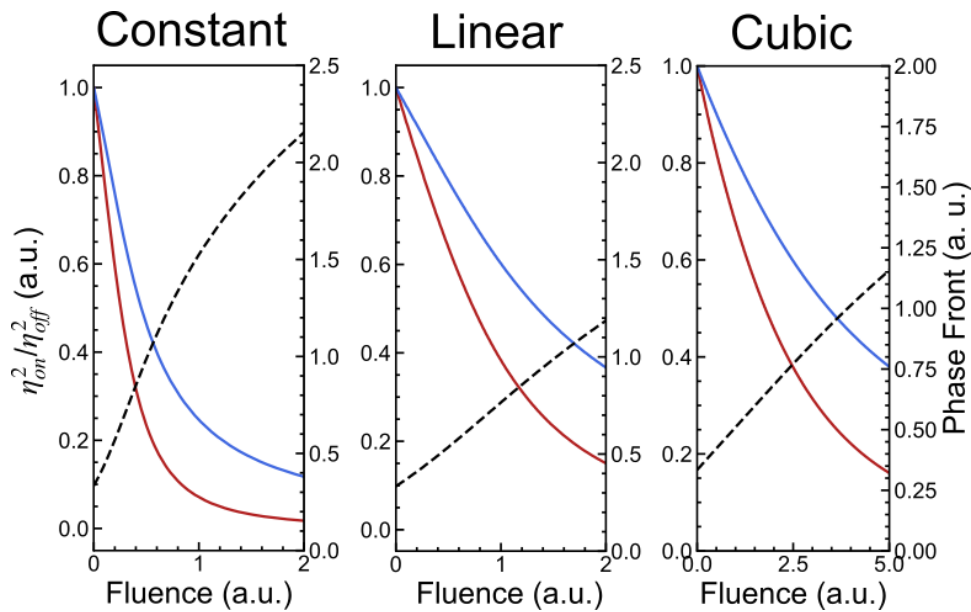


Supplementary Figure S6: Temperature dependence of the inhomogeneous order parameter model.

Dashed line corresponds to the position of the ordered surface relative to the crystal surface.

Pump-induced changes are then assumed to locally change the transition temperature additively. The temperature rise is dependent on the incident fluence, which decays exponentially from the surface. We assume that both phases absorb light equally. We consider three models for translating the absorbed fluence into a temperature rise, a constant heat capacity, a linear electronic heat capacity and a cubic heat capacity, corresponding to the low temperature limit of the Debye-Waller model.

Supplementary Figure S7 shows the results of such models for two different probe penetration depths. No significant difference is found. The main difference results from the fact that the same applied fluence results in different temperature jumps, but the overall shape is similar. In all cases the main observation, that the shorter penetrating probe reaches saturation sooner, is the same. These results were also robust to changes in the spatial dependence of T_c and the main requirement is that the surface must already show melting. When the phase front is linear with fluence, the data can be scaled to compensate for the penetration depth difference as shown in Supplementary Figure S4d.

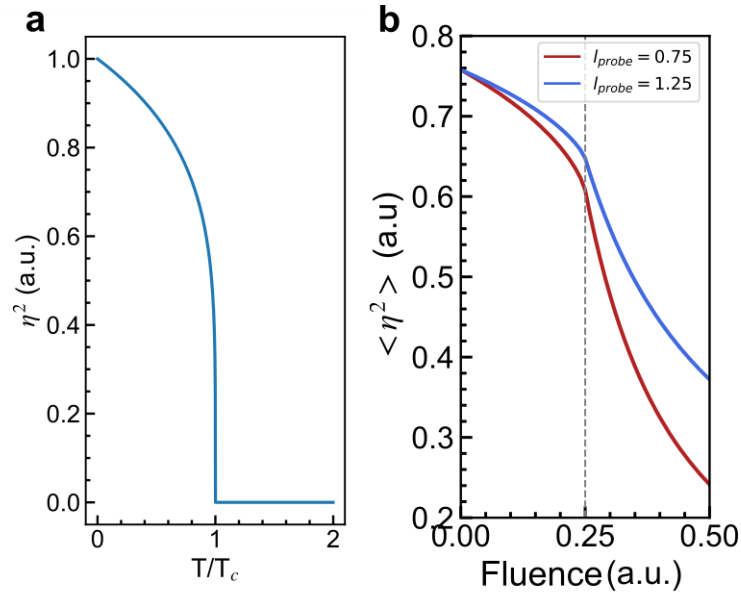


Supplementary Figure S7: Modelling the spatial dependence of the local temperature. We consider three cases. The case of a constant heat capacity, the temperature rise is linear with fluence $T(x, F) = T_0 + aFe^{-x/l_{pump}}$. The case of a heat capacity that is linear in temperature (an electronic heat capacity) the temperature rise follows a square root dependence $T(x, F) = T_0\sqrt{1 + bFe^{-x/l_{pump}}}$. Finally we also consider a heat capacity that depends cubically with temperature, corresponding to the low temperature limit of the Debye-Waller model, in which case the temperature rise is $T(x, F) = T_0(1 + cFe^{-x/l_{pump}})^{\frac{1}{4}}$

An initially homogenous 2nd order phase transition

For comparison, we use a homogenous second order model that has been previously used to characterize dynamical phase transitions. In this case, the value of the order parameter, locally, is initially independent of position in the crystal. The smooth transition results from the fact that the local (and global) order parameter size varies as $\eta^2 \propto |T - T_c|^p, T < T_c$. The average order parameter is measured in calculated in the same way as the inhomogenous first-order case and the temperature

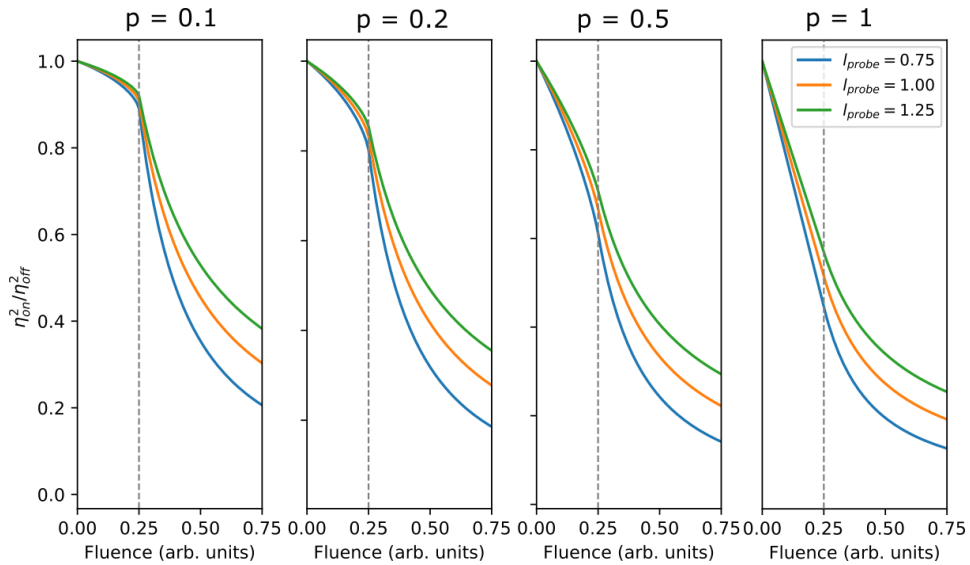
dependence is shown in Supplementary Figure S8a. The value of p is chosen ($p=0.2$) to resemble the inhomogeneous first-order case, but the following results are qualitatively similar for reasonable values of p around this value (Supplementary Figure S9).



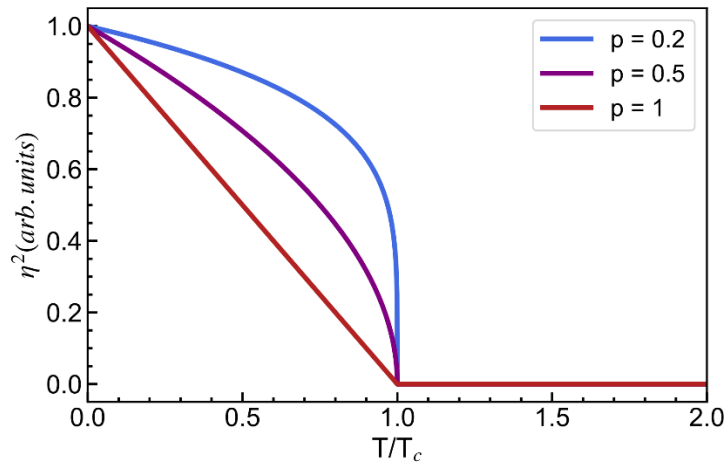
Supplementary Figure S8: Modelling a homogeneous 2nd order phase transition. **a** Temperature dependence of the order parameter in the homogeneous 2nd order transition model. **b** Sampled order parameter as a function of fluence for probes with different penetration depth. Dashed line indicates where part of the sample first reaches T_c .

We then change the local temperature in the same way as for the inhomogeneous model. As for the homogeneous model, the results were qualitatively the same for different models of the heat capacity, thus we only show the case of a constant heat capacity. The resulting fluence dependence is shown in Supplementary Figure S8b. An initial decrease is observed in which the order parameter at the surface is partially suppressed. At a critical fluence a strong discontinuity is observed which corresponds to the first time part of the sample goes above T_c . As the hottest point is always the surface of the crystal. This point is seen at the same fluence independent of the probe wavelength. The probe wavelength only defines the magnitude of the effect, with more surface sensitive colours showing a larger change. This kink is not observed in the experimental data shown in Figure 4d. However, as shown in Supplementary Figure S9, the contrast of this kink is reduced progressively as the value of p increases towards 1. Higher signal-to-noise may be required to observe the kink if the transition was described by a critical exponent significantly higher than the thermal one.

The value of the critical exponent does, however, strongly affect the temperature dependence of the order parameter (Supplementary Figure S10), with values closer to 1 resulting in a behaviour that differs greatly from the observed in Figure 2d. This means that, in order to represent our measurements within TDGL, a different critical exponent is needed for the static and dynamical phase transitions.



Supplementary Figure S9: Effect of the critical exponent on fluence dependence. For values of p around 0.2 the kink is always observed at the same fluence for any probe penetration length l . However, the contrast of the kink is progressively reduced as p is increased towards 1.



Supplementary Figure S10: Effect of the critical exponent on temperature dependence. The value of p affects the temperature dependence of the order parameter in a homogeneous second order transition.

Bibliography

1. Johnson, A. S., Amuah, E. B., Brahms, C. & Wall, S. Measurement of 10 fs pulses across the entire Visible to Near-Infrared Spectral Range. *Sci. Rep.* **10**, 4690 (2020).

